Article

Data Enhancement via Low-Rank Matrix Reconstruction in Pulsed Thermography for Carbon-fiber-Reinforced Polymers

Samira Ebrahimi [1] , **Julien Fleuret** [1] , **Matthieu Klein** [2] , **Louis-Daniel Théroux** [3] , **Clemente Ibarra-Castanedo** [1,2,*] and **Xavier Maldague** [1]

1   Computer Vision and Systems Laboratory (CVSL), Department of Electrical and Computer Engineering, Laval University, Quebec City, QC G1V 0A6, Canada; samira.ebrahimi.1@ulaval.ca (S.E.); julien.fleuret.1@ulaval.ca (J.F.); Xavier.Maldague@gel.ulaval.ca (X.M.)
2   Visiooimage Inc. Infrared Thermography Testing Systems, Quebec City, QC G1W 1A8, Canada; matthieu.klein@visiooimage.com
3   Centre Technologique et Aérospatial (CTA), Saint-Hubert, QC 3Y 8Y9, Canada; louis-daniel.theroux@cegepmontpetit.ca
*   Correspondence: samira.ebrahimi.1@ulaval.ca

Abstract: Pulsed thermography is a commonly used non-destructive testing method, and is increasingly studied for advanced materials such as carbon fiber-reinforced polymer (CFRP) evaluation. Different processing approaches are proposed to detect and characterize anomalies that may be generated in structures during the manufacturing cycle or service period. In this study, we used a type of matrix decomposition using Robust-PCA via Inexact-ALM in our experiment. We investigate this method as a pre-and post-processing method on thermal data acquired by pulsed thermography. We employed state-of-the-art methods, i.e., PCT, PPT, and PLST, as the main process. The results indicate that pre-processing on thermal data can elevate the defect detectability while post-processing, in some cases, can deteriorate the results.

Keywords: Robust PCA, RPCA, PCP, IALM, Noise Reduction, Pulsed Thermography, CFRP

Publisher's Note: MDPI stays neutral with regard to jurisdictional claims in published maps and institutional affiliations.

1. Introduction

Due to the unique features of Carbon-fiber-reinforced polymers (CFRP) - low density and high performance of Physico-chemical properties - the interest of usage and replacement with the conventional materials (Steel, aluminum,..) are increased for lighter products. The increasing demand for CFRP structures in the aerospace industry is leading to enhance more eco-efficient manufacturing development [1]. Although composite materials are sensitive to impact damage during a lifetime (manufacturing, operations, or maintenance) [2], they are less prone to corrosion and cracks than other materials. Due to different types of defects during the manufacturing process or service life of the components, it is important to monitor their efficiency and functionality non-invasively. Among non-destructive testing techniques, Infrared thermography, which is mapping the surface temperatures, can characterize the surface and sub-surface anomalies. Pulsed thermography (PT) is a no-contact and full-field IRNDT approach based on thermal heat transfer analysis during the cooling period; after the thermal impulse, an incident to the sample's surface becomes a thermal wave due to conduction, and propagates through the material. The temperature decay is recorded by the infrared camera during the cooling period. Subject to the presence of discontinuity, depending on its material and thermal properties and depth, defects will be revealed at different times. The deeper defects appear later with lower thermal contrast. In order to obtain quantitative information from thermal data, several approaches have been proposed. Manipulating thermal data makes active thermography an attractive and powerful approach for industrial control and maintenance purposes.

Moreover, effective pre-processing or post-processing can provide favorable conditions to enhance defect information extraction. Most of the pre-processing for thermal data is limited to removing the first few frames from the beginning of the sequences, cropping the image, and selecting the region of interest (ROI). Fleuret et al. [3], in their study, proved that using LatLRR (Latent Low-Rank Representation) as a post-processing

tool on the best image of state-of-the-art methods provides significant improvement in detection. Khodayar et al. [4] have used the Thermographic Signal Reconstruction (TSR) [5] approach for pre-processing to reduce the noise. They stated that PCT [6] application after the noise reduction could enhance the results. Wang et al. [7] used sequence differential pre-processing, which was combined with CIS [8] o provide better thermal data for post-processing approaches in laser infrared thermography. They evaluated the quality of the image after the combination of pre-processing with PPT [9] , or PCT and found that pre-processing improved some results. In this study, we investigate the application of a low-rank matrix from RPCA-PCP via Inexact ALM as pre-and post-processing. To evaluate our approach among the methods available in the literature, we selected the PPT, PCT, and PLST. We chose these methods due to the large number of studies that use them. Several state-of-the-art IRNDT methods, i.e., PPT, PCT, and PLST [10,11] , have been chosen to evaluate the approaches.

In the remainder of this paper, we detail the many aspects of our investigations in section 2. Section 3 demonstrates the obtained results, which we analyze and discuss in section 4. Finally, section 5 concludes this study.

2. Method and Material

2.1. Robust Principal Component Analysis (RPCA)

The Robust PCA problem can be solved via convex optimization that minimizes a combination of the nuclear norm and the ℓ^1-norm. Augmented Lagrange multiplier (ALM) is a method to solve this convex program. Equation 1 introduces the general method of ALM for solving constrained optimization problems [12]:

$$\min f(\mathbf{X}), \; subject \; to \; h(\mathbf{X}) = 0 \tag{1}$$

where $f : \mathbb{R}^n \rightarrow \mathbb{R}$ and $h : \mathbb{R}^n \rightarrow \mathbb{R}^m$. Candès et al. [13] used a convex optimization; the formulation they have used is known as PCP. The observation matrix D is assumed to be a combination of low-rank (A) and sparse matrix (E):

$$\mathbf{D} = \mathbf{A} + \mathbf{E} \tag{2}$$

To minimize the energy function ℓ_0-norm is used.

$$\min_{A,E} \; rank(\mathbf{A}) + \lambda \|\mathbf{E}\|_0 \tag{3}$$
$$subject \; to \; \mathbf{D} - \mathbf{A} - \mathbf{E} = 0$$

where λ is a positive and arbitrary balanced parameter to determine the contribution of $\mathbf{A}$ and $\mathbf{E}$ in minimizing the objective function. Since equation 3 is an NP-hard problem, i.e., at least as hard as the hardest problems in non-deterministic polynomial (NP) time, Candès et al. [13] reformulated this equation into a similar convex optimization problem as follows:

$$X = (\mathbf{A}, \mathbf{E}) \; , \min_{\mathbf{A},\mathbf{E}} (\|\mathbf{A}\|_* + \lambda \|\mathbf{E}\|_1) \tag{4}$$
$$subject \; to \; \mathbf{D} - \mathbf{A} - \mathbf{E} = 0$$

where $\|A\|_*$, $\|E\|_1$ are the nuclear norm of $\mathbf{A}$ and l_1-norm of $\mathbf{E}$, respectively. The balance parameter λ is defined as:

$$\lambda = 1/\sqrt{\max(m,n)} \tag{5}$$

The low-rank minimization due to correlation between the frames provides a framework for background modeling. Lin et al. [14] solved equation 4 using a generic ALM method. The Lagrange function can be defined as:

$$L(\mathbf{X}, \mathbf{Y}, \mu) = f(\mathbf{X}) + \langle \mathbf{Y}, h(\mathbf{X}) \rangle + \frac{\mu}{2} \|h(\mathbf{X})\|_F^2 \tag{6}$$

The Lagrange function of equation 4 is defined as:

$$L(\mathbf{A}, \mathbf{E}, \mathbf{Y}, \mu) = \|\mathbf{A}\|_* + \lambda \|\mathbf{E}\|_1 + \langle \mathbf{Y}, \mathbf{D} - \mathbf{A} - \mathbf{E}\rangle + \frac{\mu}{2}\|\mathbf{D} - \mathbf{A} - \mathbf{E}\|_F^2 \tag{7}$$

where $\mathbf{Y}$ is the Lagrange multiplier and the penalty parameter μ is a positive scalar parameter. The Inexact augmented Lagrange multiplier (IALM) method used to solve the RPCA problem is shown in Algorithm 1. $\mathbf{Y_0}$ has been initialized to $\mathbf{Y_0} = \mathbf{D}/J(\mathbf{D})$ [15], making the objective function value $\langle \mathbf{Y_0}, \mathbf{D}\rangle$ reasonably large. In addition, $J(\mathbf{D}) = max(\|\mathbf{A}\|_2, \lambda^{-1}\|\mathbf{Y}\|_\infty)$, where $\|.\|_\infty$ is the maximum absolute value of the input matrix.

In Step 1 of Algorithm 1, ρ is the learning rate and μ_0 is the initialization of the penalty parameter that influences the convergence speed. In [14], it is proven that the objective function of the RPCA problem (Equation (4)), which is non-smooth, has an excellent convergence property. In addition, it has been proven that, to converge to an optimal solution $(\mathbf{A}^*, \mathbf{E}^*)$ of the RPCA problem, it is necessary for μ_k to be non-decreasing and $\sum_{k=1}^{+\infty} \mu_k^{-1} = +\infty$. In the next section, we illustrate our experiments and data.

Algorithm 1: RPCA via IALM method

Input: Data: $\mathbf{D} \in \mathbb{R}^{m \times n}$, balance parameter λ

1   $\mathbf{Y}_0 = \frac{\mathbf{D}}{J(\mathbf{D})}; E_0 = 0; \mu_0 > 0; \rho > 1; k = 0;$

2   **while** *not converged* **do**

    // Lines 3-4 update A by solving $\mathbf{A}_{k+1} = \underset{\mathbf{A}}{argmin}\ L(\mathbf{A}, E_k, Y_k, \mu_k)$

3     $(\mathbf{U}, \mathbf{S}, \mathbf{V}) = svd(\mathbf{D} - \mathbf{E}_k + \mu_k^{-1}\mathbf{Y}_k);$

4     $\mathbf{A}_{k+1} = \mathbf{U}\mathcal{S}_{\mu_k^{-1}}[\mathbf{S}]\mathbf{V}^T;$

    // Line 5 update E by solving $\mathbf{E}_{k+1} = \underset{\mathbf{E}}{argmin}\ L(\mathbf{A}_{k+1}, \mathbf{E}, \mathbf{Y}_k, \mu_k)$

5     $\mathbf{E}_{k+1} = \mathcal{S}_{\lambda\mu_k^{-1}}[\mathbf{D} - \mathbf{A}_{k+1} + \mu_k^{-1}\mathbf{Y}_k];$

6     $\mathbf{Y}_{k+1} = \mathbf{Y}_k + \mu_k(\mathbf{D} - \mathbf{A}_{k+1} - \mathbf{E}_{k+1});$

7   *Update* μ_k *to* $\mu_{k+1};$

8     $k \leftarrow k + 1;$

9 **end**

Output: $(\mathbf{A}_k, \mathbf{E}_k)$

2.2. Data acquisition

The experiments were carried out on an academic CFRP plate (30.8 cm x 46 cm x 2.57 mm) with 73 defects of three different types, i.e., 23 round flat-bottom holes (FBH), 25 triangular Teflon inserts, and pullouts. The defects vary in size, depth, and thickness and are presented in table 1, and the schematic of the plate shows their respective locations in Figure 1a. The PT experimental setup, two flash lamps for 5ms sent a thermal pulse (6.4KJ/flash (Balcar, France)) to the specimen; a cooled infrared camera (FLIR Phoenix (FLIR Systems, Inc., Oregon, USA), InSb, midwave, 3–5 mm, Stirling Cooling) with a frame rate of 180 Hz was adopted to record the temperature profile in reflection mode (Figure 1b). The data processing was performed on a PC with 56GB memory and an Intel(R) Core(TM) i7-4820K control processing unit.

(a)

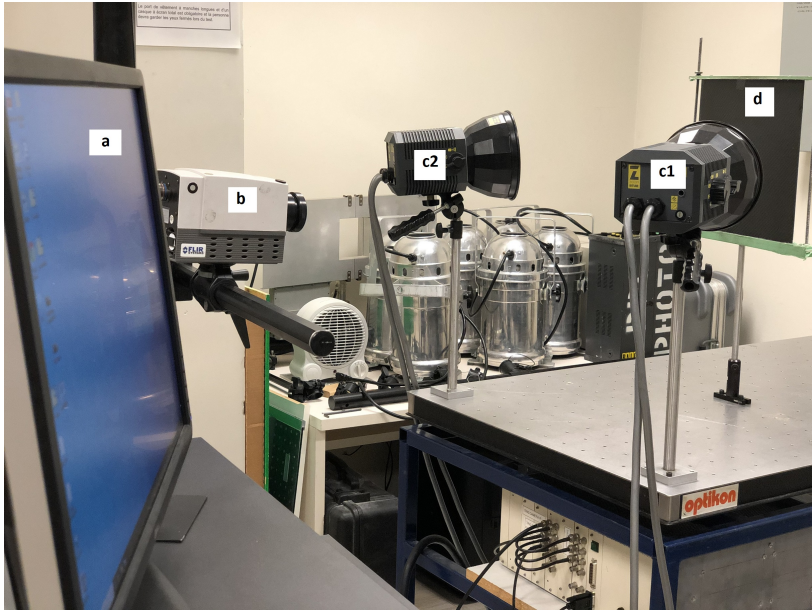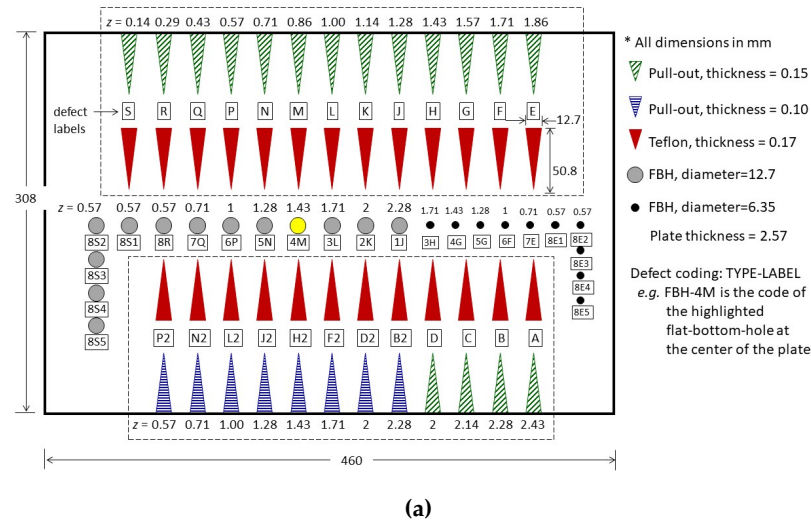**(b)**

Figure 1. (**a**) CTA CFRP plate, where Z is the defect depth and labels are used to identify the location of each defect; and (**b**) pulsed thermography setup. a, PC; b, IR camera; c1 and c2, left and right flashes; d, CFRP specimen.

Table 1. Defect specifications for the CFRP Plate, Z is the depth of the defect below the inspected surface. Thickness is the defect thickness or thickness of the holes in case of the FBH type of defect.

Defect Code	Z [mm]	Dimensions [mm]	Thickness [mm]	Defect Code	Z [mm]	Dimensions [mm]	Thickness [mm]	Defect Code	Z [mm]	Dimensions [mm]	Thickness [mm]
Teflon Inserts				Pull-Outs				FlatBottom Holes			
Tef-A	2.43	12.7×50.8	0.17	PO15-A	2.43	12.7×50.8	0.15	FBH-1J	2.28	12.70	0.29
Tef-B	2.28	12.7×50.8	0.17	PO15-B	2.28	12.7×50.8	0.15	FBH-2K	2.00	12.70	0.57
Tef-C	2.14	12.7×50.8	0.17	PO15-C	2.14	12.7×50.8	0.15	FBH-3L	1.71	12.70	0.86
Tef-D	2.00	12.7×50.8	0.17	PO15-D	2.00	12.7×50.8	0.15	FBH-4M	1.43	12.70	1.14
Tef-E	1.86	12.7×50.8	0.17	PO15-E	1.86	12.7×50.8	0.15	FBH-5N	1.28	12.70	1.29
Tef-F	1.71	12.7×50.8	0.17	PO15-F	1.71	12.7×50.8	0.15	FBH-6P	1.00	12.70	1.57
Tef-G	1.57	12.7×50.8	0.17	PO15-G	1.57	12.7×50.8	0.15	FBH-7Q	0.71	12.70	1.86
Tef-H	1.43	12.7×50.8	0.17	PO15-H	1.43	12.7×50.8	0.15	FBH-8R	0.57	12.70	2.00
Tef-J	1.28	12.7×50.8	0.17	PO15-J	1.28	12.7×50.8	0.15	FBH-8S1	0.57	12.70	2.00
Tef-K	1.14	12.7×50.8	0.17	PO15-K	1.14	12.7×50.8	0.15	FBH-8S2	0.57	12.70	2.00
Tef-L	1.00	12.7×50.8	0.17	PO15-L	1.00	12.7×50.8	0.15	FBH-8S3	0.57	12.70	2.00
Tef-M	0.86	12.7×50.8	0.17	PO15-M	0.86	12.7×50.8	0.15	FBH-8S4	0.57	12.70	2.00
Tef-N	0.71	12.7×50.8	0.17	PO15-N	0.71	12.7×50.8	0.15	FBH-8S5	0.57	12.70	2.00
Tef-P	0.57	12.7×50.8	0.17	PO15-P	0.57	12.7×50.8	0.15	FBH-3H	1.71	6.35	0.86
Tef-Q	0.43	12.7×50.8	0.17	PO15-Q	0.43	12.7×50.8	0.15	FBH-4G	1.43	6.35	1.14
Tef-R	0.29	12.7×50.8	0.17	PO15-R	0.29	12.7×50.8	0.15	FBH-5G	1.28	6.35	1.29
Tef-S	0.14	12.7×50.8	0.17	PO15-S	0.14	12.7×50.8	0.15	FBH-6F	1.00	6.35	1.57
Tef-B2	2.28	12.7×50.8	0.17	PO10-B2	2.28	12.7×50.8	0.10	FBH-7E	0.71	6.35	1.86
Tef-D2	2.00	12.7×50.8	0.17	PO10-D2	2.00	12.7×50.8	0.10	FBH-8E1	0.57	6.35	2.00
Tef-F2	1.71	12.7×50.8	0.17	PO10-F2	1.71	12.7×50.8	0.10	FBH-8E2	0.57	6.35	2.00
Tef-H2	1.43	12.7×50.8	0.17	PO10-H2	1.43	12.7×50.8	0.10	FBH-8E3	0.57	6.35	2.00
Tef-J2	1.28	12.7×50.8	0.17	PO10-J2	1.28	12.7×50.8	0.10	FBH-8E4	0.57	6.35	2.00
Tef-L2	1.00	12.7×50.8	0.17	PO10-L2	1.00	12.7×50.8	0.10	FBH-8E5	0.57	6.35	2.00
Tef-N2	0.71	12.7×50.8	0.17	PO10-N2	0.71	12.7×50.8	0.10				
Tef-P2	0.57	12.7×50.8	0.17	PO10-P2	0.57	12.7×50.8	0.10				

2.3. Metrics

In this section, we added two metrics, one to yield a thermal score indicating thermal anomalies; another to measure the segmentation potential.

2.3.1. Contrast to Noise Ratio (CNR)

The Signal-to-noise ratio (SNR) is a metric that quantitatively assesses desired signal quality by estimating the signal level with respect to the background noise. The Contrast-to-noise ratio (CNR) is similar to SNR, although it measures the image quality based on the contrast between a defective area and its neighborhood. Usamentiaga [16] proposed a definition of SNR, which is more robust against noise and image enhancement operations. Equation 8 shows this definition which has been used in this study. For this purpose, two areas are considered: an area in the defect area (carea) and a region around the defect region as a reference region (narea).

$$CNR = \frac{\mid \mu_{carea} - \mu_{narea} \mid}{\sqrt{\frac{(\sigma_{carea}{}^2 + \sigma_{narea}{}^2)}{2}}} \qquad (8)$$

where μ_{carea} and μ_{narea} are the average levels of contrast in carea and narea, respectively; σ_{carea} and σ_{narea} are the standard deviation of the contrast in carea and narea, respectively.

2.3.2. Jaccard similarity coefficient score

The Jaccard similarity coefficient [17] (also known as Jaccard index or Intersection-Over-Union (IoU)), is a statistical method that emphasizes the similarity between two finite data sets (as illustrated in Figure 2):
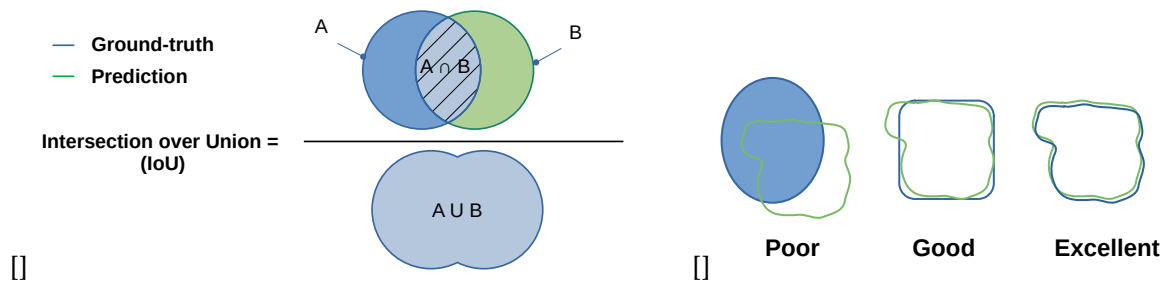
Figure 2. (**a**) Jaccard Index similarity definition; and (**b**) similarity between the ground-truth and the detected area.

This approach mathematically represents Equation 9 and is formally defined as the number of the shared members/pixels between two sets (intersection), divided by the total number of members in either set (union), multiplied by 100. $J(\mathbf{A}, \mathbf{B})$ provides a value between 0 (no similarity) and 1 (identical sets). Hence, the higher the value of IoU, the higher the level of similarities between the two sets (Figure 2b).

$$J(\mathbf{A}, \mathbf{B}) = \frac{|\mathbf{A} \cap \mathbf{B}|}{|\mathbf{A} \cup \mathbf{B}|} = \frac{|\mathbf{A} \cap \mathbf{B}|}{|\mathbf{A}| + |\mathbf{B}| - |\mathbf{A} \cap \mathbf{B}|}$$
$$0 \leq J(\mathbf{A}, \mathbf{B}) \leq 1$$
(9)

For the remainder of this article we will refer to the low-rank matrix $\mathbf{A}$ as Low-Rank Matrix (LRM).

2.4. Analysis

The previous section recalls the RPCA we used in our experiments. As described in Figures 3a and 3b we conducted two experiments. The main difference between our experiments is that: in the first experiment (Figure 3a) the LRM is computed directly from the raw-data; while in the second (Figure 3b) the LRM is computed from the output of the processing methods. For the remainder of this article we refer to the first experiment as a pre-processing experiment, and to the second as a post-processing experiment.
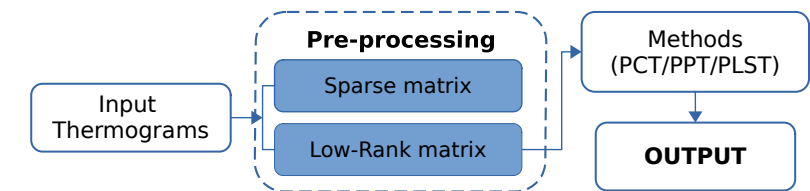
(**a**) Using method for pre-processing
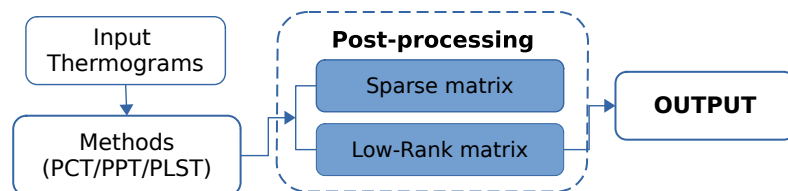
(**b**) Using method for post-processing

Figure 3. (*a*), (*b*) Pre- and post- processing methods using low-rank matrix

We chose to compare our approach with three state-of-the-art approaches, Principal Component Thermography (PCT)[6,18], Pulsed Phase Thermography (PPT) [9], Partial Least-Squares Thermography (PLST) [10,11], due to the popularity and simplicity of these methods.

The metrics are computed using different protocols. The defective and sound areas were labeled, as can be seen in Figure 4 so as to estimate the CNR score. According to Equation 8 and the labeled regions, the average and standard deviation values are obtained for all data.

Regarding the second metric, Figure 5 depicted the automatic segmentation approach and Jaccard index calculation. In our segmentation approach, after the image's contrast correction, a bilateral filter [19] smoothed the image. Then, after applying local thresholding, the small artifacts are removed from the image. The obtained mask from the segmentation step can be compared with the ground truth in order to compute the metric score.
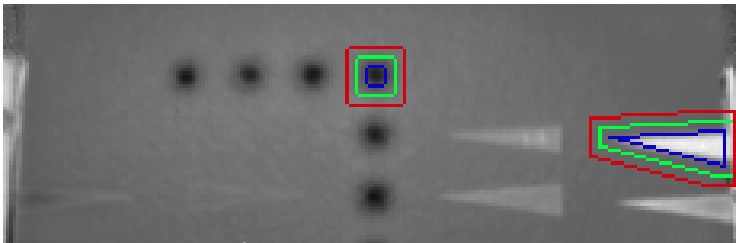

Figure 4. Examples of reference and defect regions. The boundaries of the reference region are between the green and red lines whilst the defective region is inside the blue line area
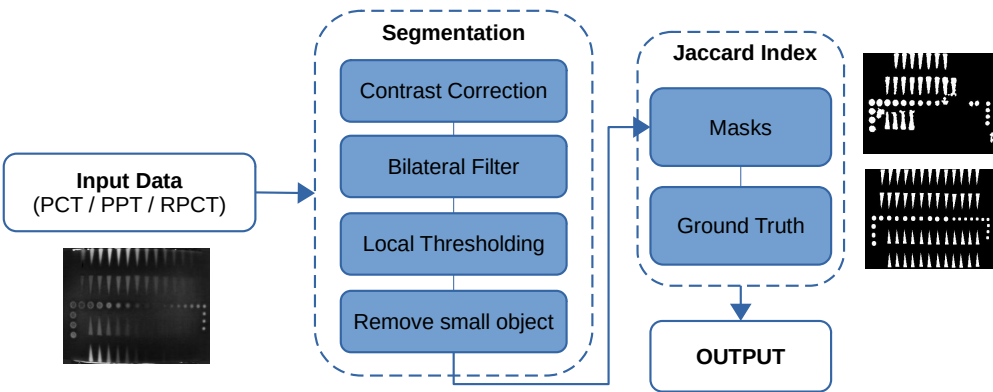
Figure 5. Segmentation and Jaccard index computation flow graph

3. Results

The original data from pulsed thermography (raw data) is used as pre- and post-processing for different processing approaches. Figure 6 shows some representative results (selected arbitrarily) of the different methods. The first column in Figure 6 results from different techniques on raw data, the second column presents RPCA results as a pre-processing method, and the last column shows the RPCA approach used as a post-processing method.

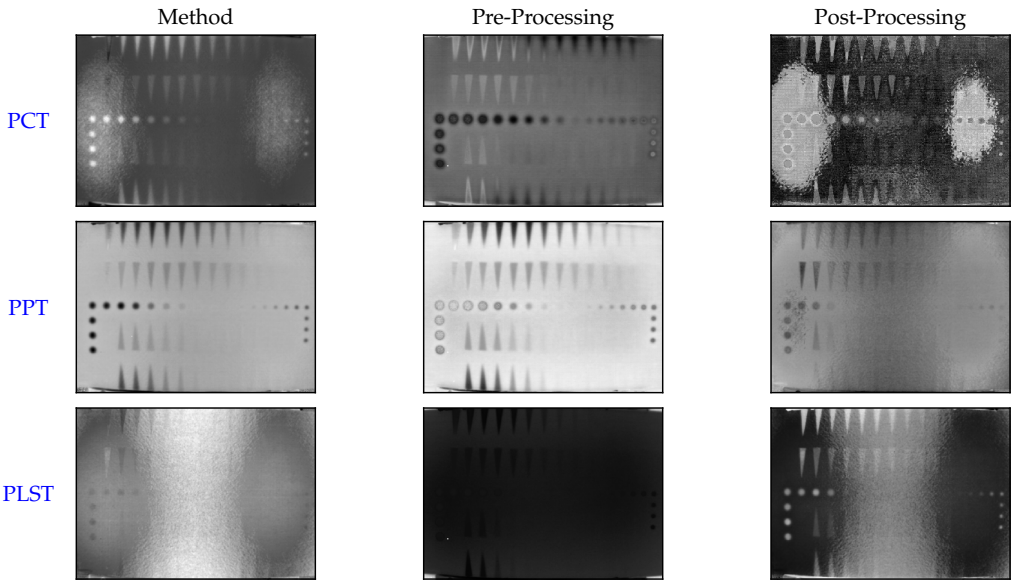| Method	Pre-Processing	Post-Processing

Figure 6. (*1st row*) These images present the 3rd component of PCT data on raw data, after using a low-rank matrix for pre-processing and post-processing, respectively. (*2nd row*) These images present PPT data at 0.135 Hz on raw data, after using a low-rank matrix for pre-processing and post-processing, respectively. (*3rd row*) These images present the 3rd component of PLST data on raw data, after using a low-rank matrix for pre-processing and post-processing, respectively.

The detailed maximum CNR Values of all methods for all defect types are presented in Tables 2, 4, and 3. Figures 7, 8, 9, and 10 present the maximum CNR value in full sequences for different methods. The CNR values of all defects and all processing techniques were calculated using the defects and references areas such as the ones shown in Figure 4.
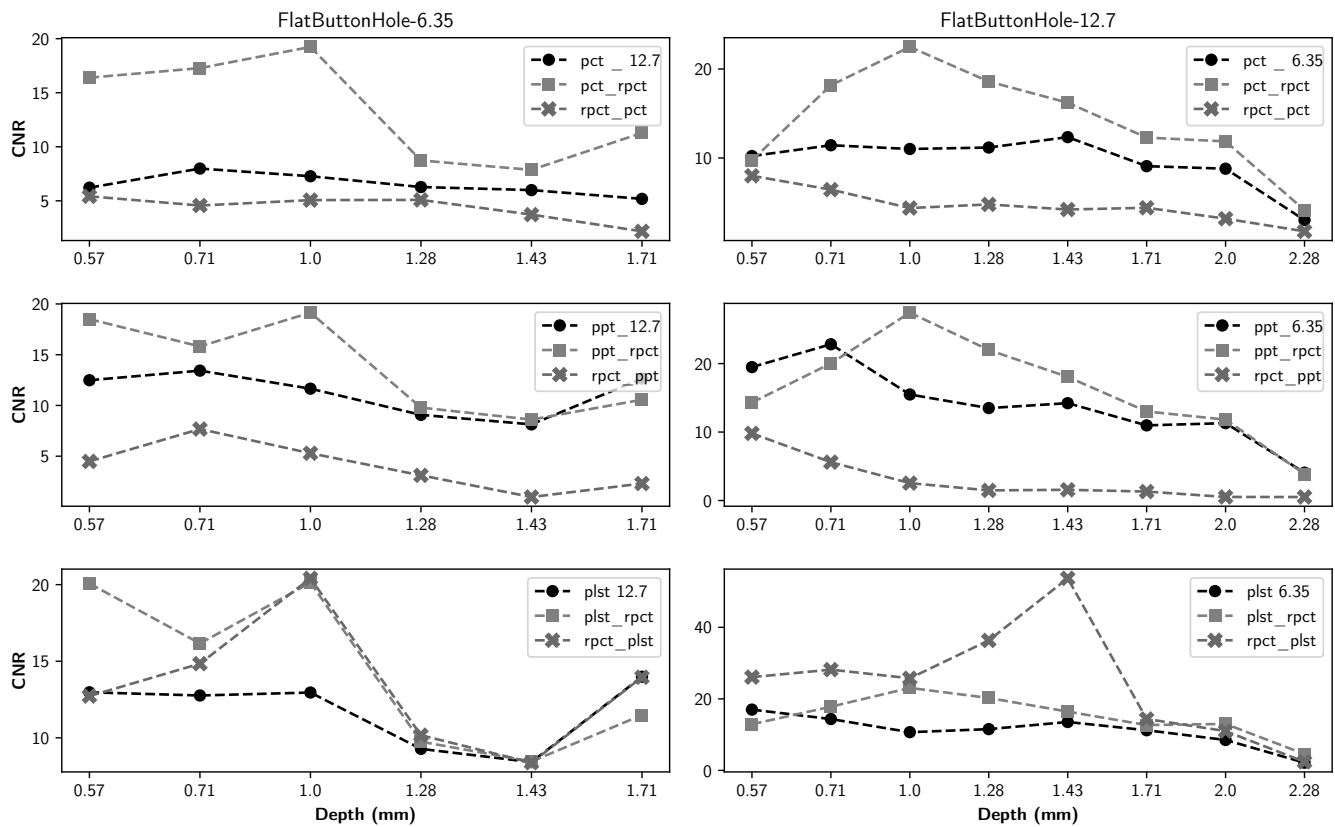
Figure 7. Maximum CNR by different FBHs as a function of defect depth for all data sequences
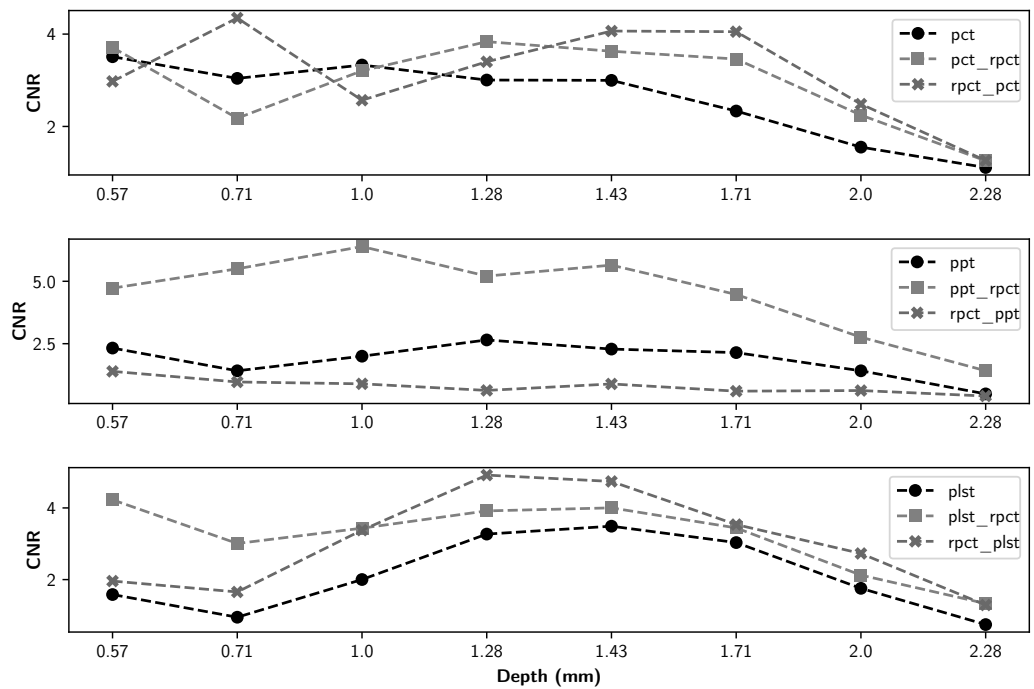

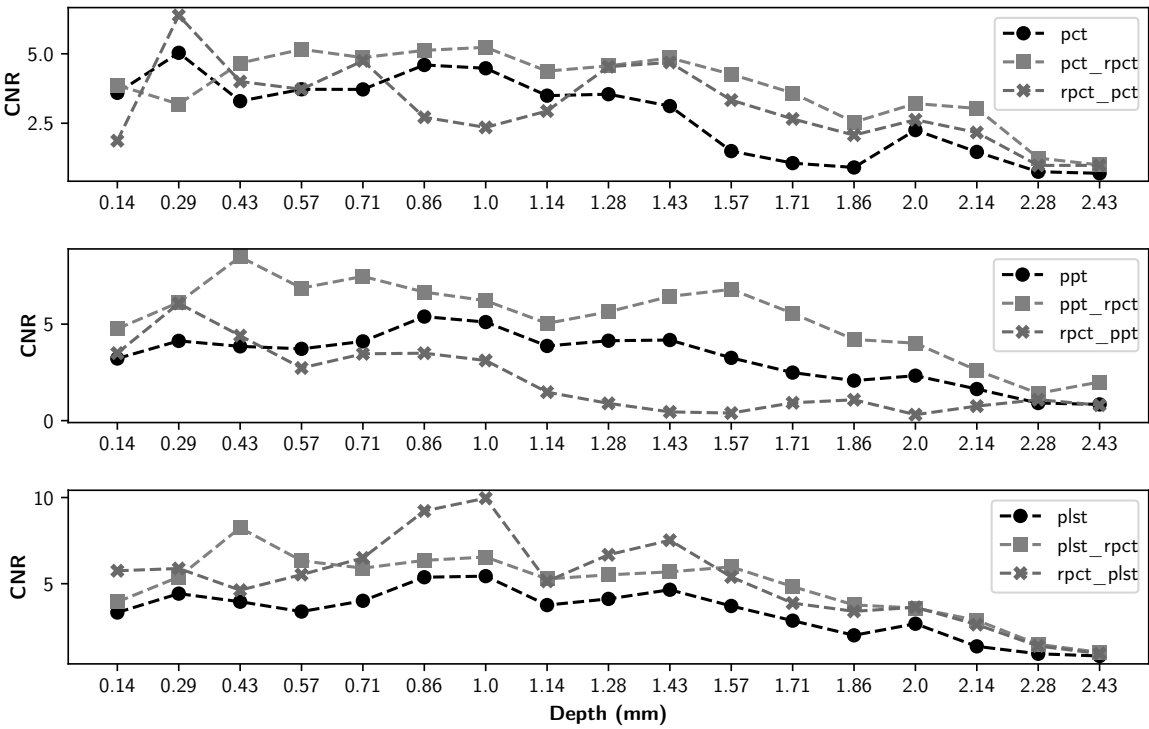**Figure 8.** Maximum CNR for pullout-10 as a function of defect depth for all data sequences

Figure 9. Maximum CNR for pullout-15 as a function of defect depth for all data sequences
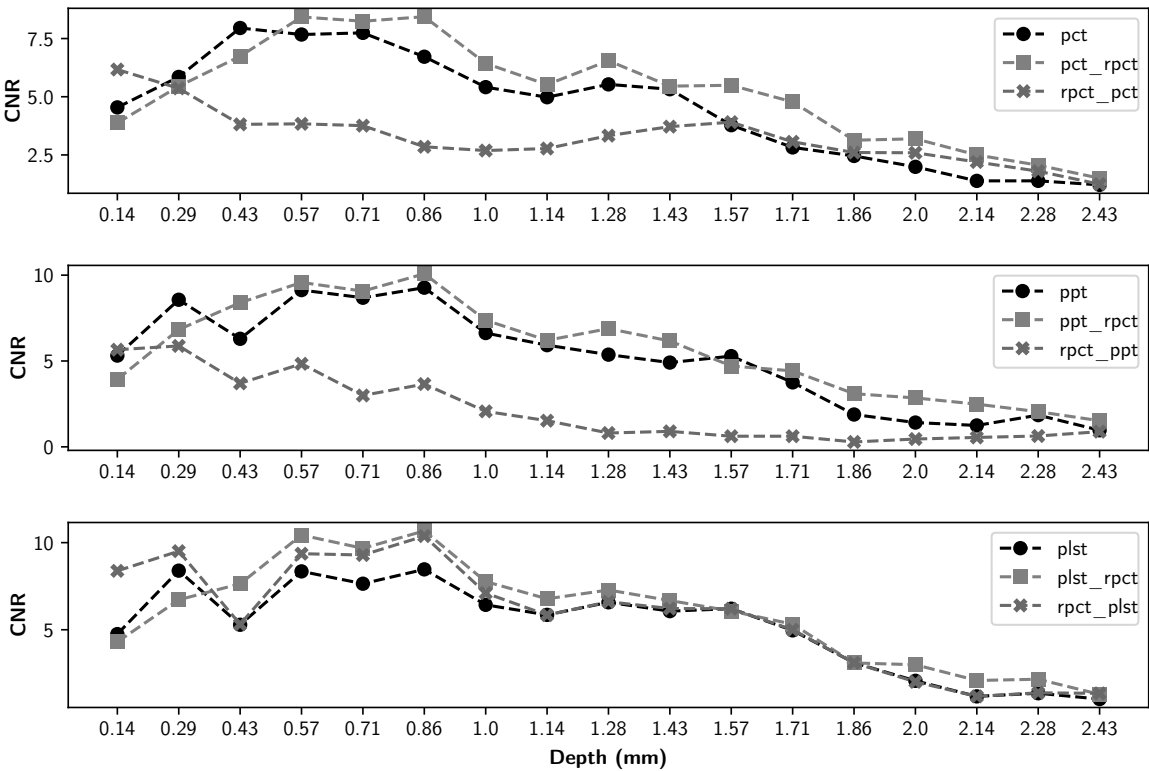

Figure 10. Maximum CNR for teflon insert as a function of defect depth for all data sequences

Table 2. Maximum CNR values for all data regarding Flat bottom holes in different depths and diameters.

			PCT					PLST					PPT				
Defect	Z	Dim.	On Raw data	Pre-P.	Post-P.	Pre-P vs. PCT	Post-P vs. PCT	On Raw data	Pre-P.	Post-P.	Pre-P. vs. PLST	Post-P. vs. PLST	On Raw data	Pre-P.	Post-P.	Pre-P. vs. PPT	Post-P. vs. PPT
FBH-8E1	0.57	6.35	6.22	16.39	5.42	163.56%	-12.87%	12.97	20.07	12.72	54.71%	-1.91%	12.48	18.50	4.48	48.18%	-64.08%
FBH-7E	0.71	6.35	7.98	17.28	4.57	116.38%	-42.82%	12.76	16.16	14.84	26.61%	16.27%	13.43	15.82	7.67	17.77%	-42.86%
FBH-6F	1	6.35	7.28	19.24	5.07	164.38%	-30.36%	12.96	20.13	20.41	55.36%	57.54%	11.65	19.15	5.29	64.32%	-54.6%
FBH-5G	1.28	6.35	6.28	8.73	5.08	39.14%	-18.99%	9.28	9.75	10.17	5.07%	9.62%	9.07	9.79	3.11	7.88%	-65.7%
FBH-4G	1.43	6.35	6	7.86	3.73	31.24%	-37.84%	8.42	8.45	8.38	0.43%	-0.49%	8.13	8.61	0.98	5.82%	-87.99%
FBH-3H	1.71	6.35	5.18	11.28	2.18	117.75%	-57.93%	13.99	11.49	13.95	-17.87%	-0.24%	12.65	10.56	2.30	-16.52%	-81.78%
FBH-8R	0.57	12.7	10.22	9.74	8	-4.67%	-21.74%	16.99	12.91	26.08	-24.06%	53.45%	19.49	14.31	9.81	-26.56%	-49.67%
FBH-7Q	0.71	12.7	11.43	18.17	6.44	58.91%	-43.64%	14.36	17.80	28.17	24%	96.18%	22.82	20.03	5.6	-12.25%	-75.47%
FBH-6P	1	12.7	11.01	22.48	4.37	104.14%	-60.29%	10.68	23.06	25.76	115.88%	141.17%	15.49	27.44	2.54	77.19%	-83.59%
FBH-5N	1.28	12.7	11.17	18.59	4.78	66.38%	-57.21%	11.53	20.25	36.35	75.59%	215.16%	13.5	21.99	1.48	62.89%	-89.05%
FBH-4M	1.43	12.7	12.35	16.22	4.21	31.35%	-65.92%	13.53	16.44	53.71	21.49%	296.9%	14.22	18.05	1.57	26.97%	-88.99%
FBH-3L	1.71	12.7	9.08	12.29	4.40	35.39%	-51.5%	11.22	12.67	14.37	12.86%	28.04%	10.97	13.01	1.31	18.51%	-88.1%
FBH-2K	2	12.7	8.79	11.86	3.18	34.85%	-63.88%	8.50	12.99	10.99	52.79%	29.22%	11.3	11.82	0.52	4.58%	-95.41%
FBH-1J	2.28	12.7	3.02	4.14	1.76	37.02%	-41.88%	2.15	4.56	2.39	112.19%	11.12%	4.06	3.87	0.51	-4.83%	-87.4%

Table 3. Maximum CNR values for all data regarding Teflon inserts in different depths and diameters.

			PCT					PLST					PPT				
Defect	Z	Dim.	On Raw data	Pre-P.	Post-P.	Pre-P vs. PCT	Post-P vs. PCT	On Raw data	Pre-P.	Post-P.	Pre-P. vs. PLST	Post-P. vs. PLST	On Raw data	Pre-P.	Post-P.	Pre-P. vs. PPT	Post-P. vs. PPT
Tef-S	0.14	12.7 x 50.8	4.54	3.88	6.17	-14.66%	35.82%	4.75	4.3	8.38	-9.45%	76.38%	5.32	3.93	5.66	-26.07%	6.41%
Tef-R	0.29	12.7 x 50.8	5.85	5.45	5.36	-6.87%	-8.39%	8.39	6.72	9.51	-19.92%	13.33%	8.57	6.83	5.88	-20.29%	-31.39%
Tef-Q	0.43	12.7 x 50.8	7.95	6.74	3.81	-15.28%	-52.04%	5.29	7.64	5.31	44.45%	0.51%	6.29	8.4	3.7	33.43%	-41.24%
Tef-P	0.57	12.7 x 50.8	7.67	8.43	3.84	9.83%	-50.01%	8.35	10.44	9.36	24.97%	12.14%	9.13	9.58	4.84	4.89%	-47.02%
Tef-N	0.71	12.7 x 50.8	7.74	8.24	3.76	6.46%	-51.48%	7.64	9.67	9.29	26.58%	21.54%	8.69	9.07	2.99	4.43%	-65.56%
Tef-M	0.86	12.7 x 50.8	6.72	8.44	2.85	25.58%	-57.58%	8.47	10.67	10.38	26.07%	22.56%	9.27	10.08	3.66	8.72%	-60.55%
Tef-L	1	12.7 x 50.8	5.41	6.43	2.69	18.86%	-50.32%	6.43	7.77	7.11	20.78%	10.52%	6.63	7.38	2.07	11.26%	-68.83%
Tef-K	1.14	12.7 x 50.8	4.98	5.52	2.78	10.87%	-44.27%	5.85	6.78	5.85	15.75%	-0.15%	5.92	6.2	1.52	4.76%	-74.28%
Tef-J	1.28	12.7 x 50.8	5.53	6.55	3.33	18.4%	-39.83%	6.58	7.28	6.61	10.72%	0.46%	5.37	6.89	0.81	28.21%	-84.99%
Tef-H	1.43	12.7 x 50.8	5.32	5.46	3.72	2.5%	-30.19%	6.07	6.68	6.22	10.05%	2.47%	4.91	6.17	0.9	25.65%	-81.63%
Tef-G	1.57	12.7 x 50.8	3.78	5.49	3.91	45.37%	3.44%	6.21	6.07	6.21	-2.21%	-0.03%	5.28	4.71	0.62	-10.9%	-88.29%
Tef-F	1.71	12.7 x 50.8	2.82	4.78	3.06	69.26%	8.54%	4.96	5.32	5	7.16%	0.75%	3.75	4.42	0.62	17.85%	-83.54%
Tef-E	1.86	12.7 x 50.8	2.46	3.13	2.6	27.47%	5.98%	3.1	3.1	3.1	-0.26%	-0.1%	1.88	3.09	0.28	64.31%	-84.92%
Tef-D	2	12.7 x 50.8	1.99	3.19	2.59	60.61%	30.41%	2.07	2.99	2.01	44.54%	-2.95%	1.41	2.85	0.46	101.45%	-67.82%
Tef-C	2.14	12.7 x 50.8	1.39	2.5	2.2	80.36%	58.63%	1.18	2.09	1.18	77.64%	0%	1.25	2.49	0.55	99.52%	-56.02%
Tef-B	2.28	12.7 x 50.8	1.39	2.06	1.8	48.47%	29.82%	1.36	2.16	1.38	59.35%	1.88%	1.85	2.05	0.63	10.86%	-65.83%
Tef-A	2.43	12.7 x 50.8	1.21	1.5	1.24	23.56%	2.39%	1.02	1.29	1.35	26.42%	32%	0.97	1.52	0.88	57.56%	-8.49%

Table 4. Maximum CNR values for all data regarding Pullouts in different depths and diameters.

			PCT					PLST					PPT				
Defect	Z	Dim.	On Raw data	Pre-P.	Post-P.	Pre-P vs. PCT	Post-P vs. PCT	On Raw data	Pre-P.	Post-P.	Pre-P. vs. PLST	Post-P. vs. PLST	On Raw data	Pre-P.	Post-P.	Pre-P. vs. PPT	Post-P. vs. PPT
PO10-P2	0.57	12.7 x 50.8	3.51	3.71	2.98	5.7%	-15.21%	1.58	4.23	1.96	167.02%	23.75%	2.33	4.73	1.391	103.23%	-40.17%
PO10-N2	0.71	12.7 x 50.8	3.04	2.18	4.35	-28.38%	42.98%	0.95	3.01	1.66	216.63%	74.21%	1.41	5.5	0.966	288.97%	-31.68%
PO10-L2	1	12.7 x 50.8	3.33	3.21	2.57	-3.75%	-22.88%	2	3.44	3.38	71.58%	68.78%	2	6.39	0.892	219.71%	-55.38%
PO10-J2	1.28	12.7 x 50.8	3.01	3.84	3.4	27.65%	13.18%	3.27	3.92	4.92	19.79%	50.34%	2.65	5.21	0.628	96.57%	-76.3%
PO10-H2	1.43	12.7 x 50.8	3	3.63	4.07	21.05%	35.62%	3.49	4	4.74	14.67%	35.79%	2.28	5.65	0.887	147.24%	-61.16%
PO10-F2	1.71	12.7 x 50.8	2.33	3.46	4.05	48.24%	73.61%	3.03	3.44	3.54	13.48%	16.58%	2.14	4.47	0.598	108.63%	-72.1%
PO10-D2	2	12.7 x 50.8	1.55	2.25	2.48	44.72%	60.05%	1.76	2.13	2.73	21.01%	55.41%	1.41	2.76	0.623	95.19%	-55.94%
PO10-B2	2.28	12.7 x 50.8	1.11	1.26	1.26	13.05%	13.59%	0.75	1.33	1.29	78.79%	73.15%	0.49	1.42	0.403	189.57%	-17.59%
PO15-S	0.14	12.7 x 50.8	3.6	3.87	1.87	7.62%	-47.93%	3.33	3.94	5.75	18.48%	72.78%	3.22	4.76	3.498	47.84%	8.67%
PO15-R	0.29	12.7 x 50.8	5.04	3.19	6.38	-36.62%	26.69%	4.42	5.39	5.88	21.79%	32.96%	4.13	6.12	6.073	48.21%	46.97%
PO15-Q	0.43	12.7 x 50.8	3.3	4.67	4	41.54%	21.42%	3.95	8.25	4.62	108.57%	16.94%	3.85	8.49	4.402	120.52%	14.37%
PO15-P	0.57	12.7 x 50.8	3.72	5.16	3.72	38.69%	0.05%	3.38	6.33	5.53	87.11%	63.41%	3.72	6.87	2.728	84.62%	-26.67%
PO15-N	0.71	12.7 x 50.8	3.72	4.86	4.75	30.8%	27.68%	4.01	5.9	6.49	47.19%	61.94%	4.11	7.47	3.462	82.03%	-15.68%
PO15-M	0.86	12.7 x 50.8	4.6	5.12	2.72	11.44%	-40.94%	5.38	6.35	9.22	18.2%	71.53%	5.39	6.66	3.494	23.54%	-35.19%
PO15-L	1	12.7 x 50.8	4.48	5.23	2.35	16.83%	-47.53%	5.44	6.55	9.96	20.38%	83.21%	5.11	6.22	3.117	21.72%	-38.97%
PO15-K	1.14	12.7 x 50.8	3.49	4.38	2.94	25.31%	-15.83%	3.76	5.28	5.14	40.36%	36.63%	3.87	5.04	1.476	30.23%	-61.86%
PO15-J	1.28	12.7 x 50.8	3.55	4.56	4.54	28.72%	27.93%	4.12	5.51	6.68	33.88%	62.17%	4.14	5.64	0.895	36.18%	-78.38%
PO15-H	1.43	12.7 x 50.8	3.12	4.85	4.69	55.61%	50.38%	4.65	5.69	7.52	22.38%	61.81%	4.18	6.44	0.453	54.13%	-89.15%
PO15-G	1.57	12.7 x 50.8	1.5	4.26	3.33	184.84%	122.65%	3.71	5.98	5.39	61.21%	45.45%	3.25	6.8	0.392	109.1%	-87.95%
PO15-F	1.71	12.7 x 50.8	1.06	3.59	2.66	237.22%	149.62%	2.86	4.83	3.88	69.32%	35.73%	2.49	5.56	0.925	123.3%	-62.84%
PO15-E	1.86	12.7 x 50.8	0.91	2.54	2.07	179.52%	128.19%	2.01	3.77	3.4	87.79%	69.29%	2.07	4.21	1.079	102.84	-47.97
PO15-D	2	12.7 x 50.8	2.25	3.21	2.63	42.41%	16.46%	2.68	3.59	3.63	34.03%	35.67%	2.33	4.01	0.309	72.26	-86.73
PO15-C	2.14	12.7 x 50.8	1.47	3.03	2.17	106.75%	47.78%	1.36	2.88	2.63	111%	92.6%	1.64	2.61	0.752	59.22	-54.09
PO15-B	2.28	12.7 x 50.8	0.75	1.25	0.98	65.25%	30.24%	0.93	1.48	1.38	58.89%	48.18%	0.91	1.41	1.085	55.04	18.97
PO15-A	2.43	12.7 x 50.8	0.7	1	0.98	43.19%	41.03%	0.81	1.01	0.95	25.84%	17.39%	0.84	2	0.802	137.81	-4.64

Figure 11a and 11b illustrate the number of enhanced defects using pre- and post-processing, respectively. The numbers inside the columns represent the enhanced defects in different techniques, and the number above the columns are the total number of defects in each case.
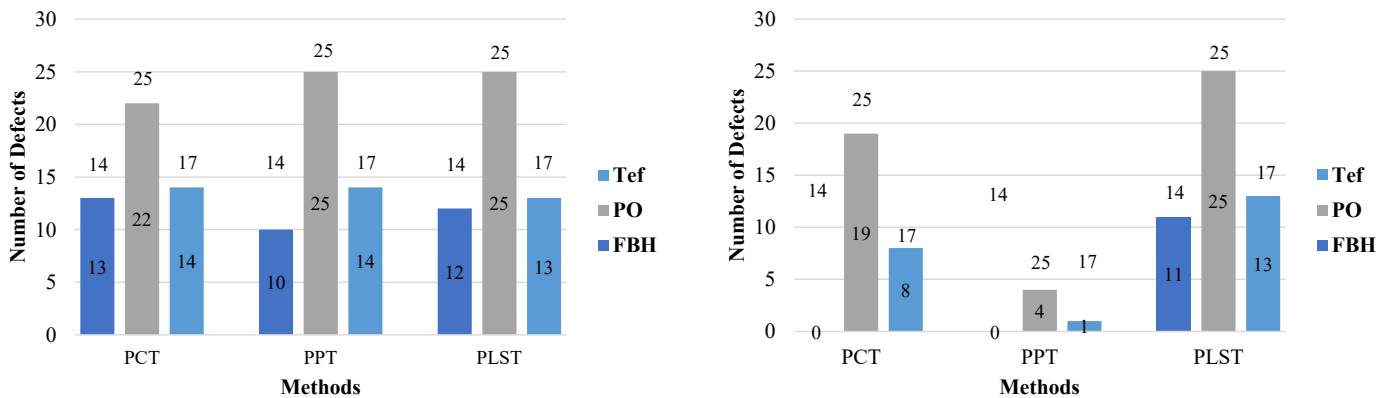
(a) Results of the pre-processing experiments.   s **(b)** Results of the post-processing experiments.

Figure 11. Number of defects which are enhanced for each experiment.

The best Jaccard index for all data sequences for different methods is shown in Table 5.

Table 5. Jaccard Index values for different methods on segmented data.

Method	On Raw Data	Pre_Processing	Post_Processing
PCT	60.43	64.08	53.94
PPT	61.19	62.82	55
PLST	50.66	55.36	55.35

o

Figure 6 illustrates selected results from different methods. In this figure, the first image from each raw presents the selected technique on raw data (PCT, PPT, or PLST); the second and third images show the effect of using the LRM as a pre- and post-processing method.

Our segmentation approach was evaluated by the Jaccard index presented in Table 5.

4. Discussion

From Table 2, one can note that the results from the pre-processing experiments are noticeably better than those obtained from the post-processing experiment. Note that these results are compared with results obtained without using low-rank matrices for both experiments. For the PCT method, one can note:

- The pre-processing experiments have led to a clear improvement of the results, regardless of the defect type. For 13 of the 14 FBH defects, one can observe an increase in the CNR score. The ratio of this improvement varies from 31.24% to 163.56%. The CNR scores obtained for the PO defects show a higher score in 22 of the 25 defects, with a ratio that varies from 0.43% to 115.88%. Similarly, the CNR scores obtained for the Teflon inserts also show a CNR score increase for 14 of the 17 defects. The ratio of this improvement varies from 2.5% to 80.36%.

- The results of the post-processing experiments do not show any improvement for the FBH defects. Nevertheless, for the PO defects, one can note that there is a higher CNR score for 19 of 25 defects. The ratio of this improvement varies from 0.05% to 149.62%.

For Teflon defects, 8 of the 17 defects have a higher CNR score, with a ratio between 2.39% to 58.63%.

From the PPT method results, one can observe:

- As already observed with the PCT, the results of the pre-processing experiments offer an improvement for every type of defect. For 10 of the 14 FBH defects, one can observe that their CNR score increases, with a ratio between: 4.58% to 77.19%. The PO defects show an increases in the CNR score for all of the defects. The ratio of improvement varies from 21.72% to 288.97%. For Teflon inserts, the number of defects with a higher CNR is similar to what was observed for the previous method, with 14 of the 17 defects with improved CNR value. The ratio of improvement varies from 4.43% to 101.45%.
- The results obtained for the post-processing experiment show very little improvement. No improvement at all was recorded for the FBH. For the PO defects, 4 of the 25 defects had an increased CNR value, with a ratio between 8.67% to 46.97%. Only one Teflon defect of the 17 defects had its CNR increased by a ratio of 6.41%.

Finally, from the PLST method results, one can note:

- The pre-processing experiments shows a similar trend as the trend observed for the two other methods. For 12 of the 14 FBH defects, CNR score increased, with a ratio from 0.43% to 115.88%. All of the PO defects have their CNR score increased, with a ratio between 13.48% to 216.63%. Finally, for the Teflon insert 13 defects of the 17 obtained an increased CNR score, with a ratio between 7.16% to 77.64%.
- For the post-processing approach, one can note that the results are quite similar to those obtained during the pre-processing experiments. For 11 of the 17 FBH defects, an increase of the CNR value was observed, with a ratio from 9.62% to 296.9%. All of the PO defects show an improvement of their CNR score, ranging from 16.98% to 92.6%. For 13 of the 17 Teflon defects, the CNR score has improved, with a ratio from 0.46% to 76.38%.

Comparing the two experiments, one can observe that the pre-processing experiment leads to a larger number of defective regions for PCT and PPT methods than the post-processing experiments. Nevertheless, this observation is not valid for the PLST method, where the results are pretty similar in both experiments. For the PO defect, the increase in terms of CNR score is higher in the pre-processing experiments; the mean ratio of improvement is 2.6 times higher than it is for the post-processing experiments. Similarly, the mean ratio of improvement for the Teflon defects is 1.7 times higher in the pre-processing experiment than in the post-processing experiments. Nonetheless, the mean improvement ratio is 2.5 times higher in the post-processing experiment than in the pre-processing experiment. To conclude, our results show that computing a LRM from the raw data before applying any state-of-the-art method significantly improves the results of the method. In the particular case of FBH defects, one can consider computing an LRM before and after the method.

As one can note in Table 5, and see in Figure 11b, using the LRM, before state-of-the-art processing method, leads to better Jaccard index scores, therefore segmentation, in all cases. One can also note that the Jaccard index score for the PLST method does not change much between the pre-processing and post-processing experiments. The Jaccard index score for the PCT and PPT methods decreases noticeably for the segmentation of the post-processing experiment results compared with the segmentation of the Raw-Data. This indicates that the results of the segmentation worsen.

5. Conclusions

The present study investigates the benefits of the low-rank matrices for pulsed thermography. The investigation conducted for this study focuses on enhancing defective regions located within a reference sample of CFRP. The sample we used has three types of defects. Two experiments were conducted: during the first one, the low-rank matrix was computed from the raw data before applying any processing. During the second experiment, the low-rank matrix is computed from the output of a method, after it was applied

on raw data. For both experiments we used PPT [9], PCT [6,18], and PLST [10,11]. Two figures of merit, the Contrast-to-Noise Ratio (CNR) and the Jaccard similarity coefficient, were used to evaluate the results quantitatively.

Our results conclude that using a low-rank matrix, when used as a pre-processing method, noticeably improves the results of all of the techniques. The low-rank matrix reconstruction effectively reduces the noise and non-uniform heating. When used as a post-processing method, the results vary from one method to another. When used on the output of PLST, the low-rank matrix reconstruction still shows better results than the PLST alone. Nonetheless, this conclusion is not shared for both PPT and PCT.

This study presents very promising results regarding the improvement of anomaly detection in pulsed thermography in CFRPs. To make the proposed approach more practical in NDT techniques, future research will be directed towards the application of pre- and post-processing to a wider range of materials.

References

1. Vo Dong, P.A.; Azzaro-Pantel, C.; Cadene, A.L. Economic and environmental assessment of recovery and disposal pathways for CFRP waste management. *Resources, Conservation and Recycling* **2018**, *133*, 63–75. doi:https://doi.org/10.1016/j.resconrec.2018.01.024.
2. Abrate, S. Impact on laminated composite materials **1991**.
3. Fleuret, J.; Ibarra-Castanedo, C.; Ebrahimi, S.; Maldague, X. Latent Low Rank Representation Applied to Thermography. Proceedings of the 2020 International Conference on Quantitative InfraRed Thermography, Porto, Portugal, 2020, pp. 21–30.
4. Khodayar, F.; Lopez, F.; Ibarra-Castanedo, C.; Maldague, X. Optimization of the inspection of large composite materials using robotized line scan thermography. *Journal of Nondestructive Evaluation* **2017**, *36*, 32.
5. Shepard, S.M. Advances in pulsed thermography. Thermosense XXIII; Rozlosnik, A.E.; Dinwiddie, R.B., Eds. International Society for Optics and Photonics, SPIE, 2001, Vol. 4360, pp. 511 – 515.
6. Rajic, N. Principal Component thermography for flaw contrast enhancement and flaw depth characterization in composite structures. *Composite Structures* **2002**, *58*, 521–528. doi:10.1016/S0263-8223(02)00161-7.
7. Wang, Q.; Hu, Q.; Qiu, J.; Pei, C.; Li, X.; Zhou, H.; Xia, R.; Liu, J. Image enhancement method for laser infrared thermography defect detection in aviation composites. *Optical Engineering* **2019**, *58*, 1 – 11. doi:10.1117/1.OE.58.10.103104.
8. Alard, C.; Lupton, R.H. A Method for Optimal Image Subtraction. *The Astrophysical Journal* **1998**, *503*, 325–331. doi:10.1086/305984.
9. Maldague, X.; Marinetti, S. Pulse phase infrared thermography. *Journal of applied physics* **1996**, *79*, 2694–2698.
10. Lopez, F.; Nicolau, V.; Maldague, X.; Ibarra-Castanedo, C. Multivariate infrared signal processing by partial least-squares thermography. ISEM Conference, 2013.
11. Lopez, F.; Ibarra-Castanedo, C.; de Paulo Nicolau, V.; Maldague, X. Optimization of pulsed thermography inspection by partial least-squares regression. *Ndt & E International* **2014**, *66*, 128–138.
12. Bertsekas, D.P. Enlarging the region of convergence of Newton's method for constrained optimization. *Journal of optimization theory and applications* **1982**, *36*, 221–252.
13. Candès, E.J.; Li, X.; Ma, Y.; Wright, J. Robust Principal Component Analysis? *J. ACM* **2011**, *58*. doi:10.1145/1970392.1970395.
14. Lin, Z.; Chen, M.; Ma, Y. The augmented lagrange multiplier method for exact recovery of corrupted low-rank matrices. *arXiv preprint arXiv:1009.5055* **2010**.
15. Candès, E.; Recht, B. Exact Matrix Completion via Convex Optimization. *Communications of the ACM* **2008**, *9*, 717–772. doi:10.1007/s10208-009-9045-5.

16.   Usamentiaga, R.; Ibarra-Castanedo, C.; Maldague, X. More than Fifty Shades of Grey: Quantitative Characterization of Defects and Interpretation Using SNR and CNR. *Journal of Nondestructive Evaluation* **2018**, *37*. doi:10.1007/s10921-018-0479-z.

17.   Jaccard, P. Lois de distribution florale dans la zone alpine. *Bulletin de la Société vaudoise des sciences naturelles* **1902**, *38*, 69–130. doi:10.5169/seals-266762.

18.   Rajic, N. Principal component thermography. Technical report, DEFENCE SCIENCE AND TECHNOLOGY ORGANISATION VICTORIA (AUSTRALIA . . . , 2002.

19.   Tomasi, C.; Manduchi, R. Bilateral filtering for gray and color images. Sixth International Conference on Computer Vision (IEEE Cat. No.98CH36271), 1998, pp. 839–846. doi:10.1109/ICCV.1998.710815.